CrystEngComm

ROYAL SOCIETY OF CHEMISTRY

PAPER

View Article Online
View Journal | View Issue

Cite this: *CrystEngComm*, 2025, **27**, 22

Dynamic manipulation of upconversion luminescence by constructing metal–organic framework and lanthanide-doped nanoparticle composites†

Huiwen Yan,‡ Wenqian Cao,‡ Zhiyu Wang, Yuanjing Cui * and Guodong Qian *

The dynamic manipulation of multi-photon upconversion, enabling rich and tunable emission colors, has generated significant interest in lanthanide-doped upconversion nanoparticles (UCNPs) about their fundamental research and frontier applications. However, manipulating photochromic upconversion emissions towards luminescent color tuning (LCT) of a single UCNP emitter without tedious endogenous regulation remains a challenging endeavor. In this study, $NaYF_4$@$NaYF_4$:*x*%Yb, 2%Er (*X* = 60, 80 and 98) was incorporated with UiO-66-type metal–organic frameworks (MOFs, including UiO-66, UiO-66-NDC, UiO-66-NH_2) by a simple and versatile *in situ* synthesis method. The UCNPs are combined with MOFs in a monodisperse state, and the stability of the composites is improved compared to UCNPs alone. Effective modulation of the upconversion luminescence (UCL) properties of UCNPs was achieved by exploiting the chemical bonds with high-energy vibrations in MOFs, which facilitates the multi-phonon relaxation (MPR) processes of Er^{3+}. Our findings enable versatile designs and dynamic control of emission colors from luminescent materials, opening up new opportunities for their advanced photonic applications, notably in optical anti-counterfeiting.

Received 13th September 2024,
Accepted 20th November 2024

DOI: 10.1039/d4ce00932k

rsc.li/crystengcomm

1. Introduction

Lanthanide-doped upconversion nanoparticles (UCNPs) are a promising new generation of optical materials. Upconversion utilizes the long lifetime of trivalent lanthanide ions embedded in a suitable inorganic host lattice and the sequential absorption of multiple photons at real step-like energy levels to convert two or more low-energy excitation photons (usually near-infrared light, NIR) into high-energy photons (*e.g.*, visible and ultraviolet light).[1–3] The efficiency of the UC process is typically several orders of magnitude higher than that of nonlinear multiphoton absorption, so UC can be generated with low-cost continuous lasers without the need to use ultrashort pulsed lasers for nonlinear multiphoton excitation.[4,5] The 4f electronic configuration of trivalent lanthanide ions showcases numerous discrete energy levels, enabling diverse energy transfer channels that govern excitation–emission dynamics and produce a vibrant range of emission colors.[6] This has triggered many studies on the optical and physical properties of UCNPs with a view to modulating their UCL by rational design to make them meet the needs of specific applications.

Currently, various strategies have been developed for modulating the luminescence properties of UCNPs. Firstly, precisely controlling the size and morphology of UCNPs, it was shown that in the $NaYF_4$:20%Yb^{3+}, 2%Er^{3+} system, Marco Kraft *et al.* found that smaller-sized NPs were more inclined to emit green light as compared to the larger ones.[7] Secondly, adjusting the concentrations of dopant ions, for example, increasing the doping amount of Yb^{3+} or Er^{3+} in UCNPs can effectively improve their red-to-green (R/G) ratio.[8–13] Thirdly, changing the types of dopant ions, *e.g.* introducing Ce^{3+} into the Yb^{3+}/Ho^{3+} system, this can lead to a change in the luminescence color of UCNPs from green to red.[14,15] All of the above methods are endogenous regulatory strategies, which mainly involve the synthesis process of UCNPs, which is a tedious and complicated step. The large surface-to-volume ratio of UCNPs enables their surfaces to become the dominant player in the complex optical pathways of lanthanide ions, including energy migration, cross-relaxation

State Key Laboratory of Silicon and Advanced Semiconductor Materials, ZJU-Hangzhou Global Scientific and Technological Innovation Center, School of Materials Science & Engineering, Zhejiang University, Hangzhou 310027, China. E-mail: cuiyj@zju.edu.cn, gdqian@zju.edu.cn

† Electronic supplementary information (ESI) available: Supplementary figures of the characterization of the as-prepared nanoparticles. See DOI: https://doi.org/10.1039/d4ce00932k

‡ These authors contributed equally to this paper.

and multi-phonon relaxation. In view of this, some surface modification methods, such as ligand exchange or ligand removal, are employed to investigate the energy transfer dynamics of UCNPs, aiming to achieve controllable upconversion emissions.[16] In current studies targeting the modulation of UCL properties of UCNPs, the approach by regulating the excitation power has been demonstrated to offer a number of significant advantages, such as exogenous control, non-invasiveness, and color versatility and tunability, which opens up the possibility of realizing customized luminescence in specific applications. However, the issue of their stability under different excitation power conditions has become a key challenge limiting their application potential. Therefore, effective control of the UCL properties by precisely adjusting the excitation power while maintaining NP stability remains a challenge.

Metal–organic frameworks (MOFs) are a class of crystalline porous materials formed by the self-assembly process of inorganic metal nodes (metal ions or metal clusters) with organically bridged ligands in a periodic and highly ordered structure. With their remarkable features such as easy synthetic pathways, structural diversity and designability, MOFs show great potential for application in many scientific and industrial fields.[17–21] It is suggested that by utilizing the abundant open active sites on the surface of MOFs, effective binding and even interaction with NPs can be achieved, which not only promotes homogeneous dispersion of NPs, but also may confer new functionalities to MOFs while influencing the properties of NPs through interaction.[22–25] The abundant and controllable functional groups of MOFs provide different energy transfer pathways for regulating the excitation–emission dynamic processes. On this basis, it can be speculated that MOFs may become ideal host materials for UCNPs, which in turn can be used to modulate the UCL properties of UCNPs.

In this study, we successfully prepared the composites of $NaYF_4$@$NaYF_4$:*x*%Yb, 2%Er (*X* = 60, 80 and 98) (abbreviated as Y@*x*Yb) with UiO-66-type MOFs (including UiO-66, UiO-66-NDC, UiO-66-NH_2) by using an *in situ* synthesis method illustrated in Scheme 1. In the composites, the surfaces of MOFs were coated with uniformly dispersed UCNPs. The experimental results showed that in the UiO-66-NH_2@Y@98Yb composite, the R/G ratio increased rapidly as the excitation power density increased from 0.34 W cm^{-2} to 2.51 W cm^{-2}, and then the ratio tended to be saturated when the power density reached about 4.58 W cm^{-2}. In addition, effective luminescent color tuning (LCT) of the composites was achieved by adjusting the excitation power density. Fortunately, the photochemical stability of the UCNPs was successfully enhanced by complexing them with MOFs. Furthermore, due to the chemical bonds with high-energy vibrations in the structure of the MOFs that promote the $^2H_{11/2}/^4S_{3/2} \rightarrow {}^4F_{9/2}$ and $^4I_{11/2} \rightarrow {}^4I_{13/2}$ multiphonon relaxation (MPR) processes of Er^{3+}, the composites preferred to emit red UCL and had significantly higher R/G ratios as compared to the pure UCNPs under the same conditions.

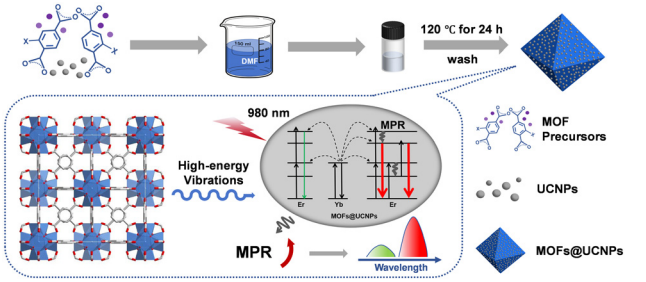

Scheme 1 Schematic of the fabrication of UCNP and MOF nanocomposites. The dashed box briefly illustrates that MOFs promote the MPR processes of Er^{3+} through chemical bonds with high-energy vibrations, resulting in an increase in the R/G ratio of the composites, which tends towards red UCL emission. Note that MOFs@UCNPs refer to the composites.

2. Experimental methods

2.1 Preparation of ~10 nm $NaYF_4$ upconversion nanoparticles

A methanol solution containing 1 mmol of $YCl_3{\cdot}6H_2O$ was first mixed with 6 mL of oleic acid (OA) and 15 mL of 1-octadecene (ODE) in a three-neck flask at room temperature. Under continuous nitrogen protection and vigorous magnetic stirring, the mixed solution was heated to 150 °C, maintained for 60 min to remove methanol by evaporation, and subsequently cooled to room temperature. Next, a methanol solution containing 4 mmol NaOH was added to the flask and stirring was continued for 30 minutes. Subsequently, the temperature of the solution was increased to 100 °C, maintained for 60 minutes to remove methanol, and again cooled to room temperature. Afterwards, a methanol solution containing 4 mmol NH_4F was added to the system, stirred for 30 minutes, and then the solution was again heated to 100 °C and held for 60 minutes to remove the methanol. After that, the solution was rapidly heated up to 300 °C in a nitrogen atmosphere and kept for 45 minutes. After the solution was cooled to room temperature, the nanoparticles were precipitated by centrifugation by adding excess ethanol to isolate the nanoparticles. The resulting nanoparticles were further washed three times using a mixture of ethanol and cyclohexane (1 : 1, v/v). Finally, the washed nanoparticles were dispersed in cyclohexane and stored at 4 °C for subsequent use.

2.2 Preparation of core–shell $NaYF_4$@$NaYF_4$:Yb/Er upconversion nanoparticles

Taking the synthesis of Y@98Yb core–shell UCNPs as an example, a methanol solution containing 0.98 mmol $YbCl_3{\cdot}6H_2O$ and 0.02 mmol $ErCl_3{\cdot}6H_2O$ was firstly mixed with 3 mL OA and 7.5 mL ODE in a three-necked flask at room temperature. The mixed solution was heated to 150 °C by vigorous magnetic stirring while under a nitrogen atmosphere, kept for 60 min to remove methanol by evaporation, and subsequently cooled to room temperature. Next, a methanol solution containing 2.5 mmol NaOH and 4

mmol NH_4F was added to the flask and stirred for 30 min before adding a pre-prepared cyclohexane solution containing 0.1 mmol of approximately 10 nm $NaYF_4$ nanoparticles and continued to stir for 10 min. Subsequently, the temperature of the solution was increased to 100 °C and held for 60 min to remove methanol and cyclohexane, and then rapidly increased to 300 °C and held for 30 min. After the solution was cooled to room temperature, the UCNPs were centrifuged and washed as described previously. Finally, the washed UCNPs were dispersed in cyclohexane and stored at 4 °C for subsequent experiments.

During the preparation of core–shell UCNPs with different Yb^{3+} contents, only the molar ratio of the corresponding $LnCl_3{\cdot}6H_2O$ needed to be adjusted while ensuring that the total amount of Ln^{3+} was 1 mmol.

2.3 Preparation of MOFs

Synthesis of UiO-66-NH_2. First, 10 mL of *N*,*N*-dimethylformamide (DMF) solution containing $ZrCl_4$ (10.2 mg, 0.044 mmol) and 2-aminoterephthalic acid (7.3 mg, 0.040 mmol) was mixed with 1.2 mL of glacial acetic acid, followed by sonication for 15 min. The mixed solution was transferred to a vial and placed in an oven at 120 °C for 24 hours. Then, the crystallized powder was isolated by filtration and the powder was washed with DMF and anhydrous methanol. Finally, the washed powder was dried and ready for use.

Synthesis of UiO-66-NDC and UiO-66. The synthesis method was similar to the preparation of UiO-66-NH_2, with the main difference being the choice of ligands. 1,4-naphthalenedicarboxylic acid (8.7 mg, 0.040 mmol) was used as the ligand for UiO-66-NDC, and terephthalic acid (6.7 mg, 0.040 mmol) was used for UiO-66. The rest of the synthesis steps remained the same as the preparation of UiO-66-NH_2.

2.4 Preparation of MOF@UCNP composites

The preparation of the composites was similar to the process of synthesizing pure MOFs. First, a precursor solution of pure MOFs was prepared. Subsequently, this precursor solution was mixed with a solution of DMF (300 μL) containing ligand-free core–shell UCNPs (0.06 mmol). The preparation of the ligand-free UCNPs is available in the ESI.† The mixed solution was sonicated for 5 min, transferred to a vial, and reacted under the same conditions as for the synthesis of MOFs. Then, the crystallized powder was separated by filtration and the powder was washed with DMF and anhydrous methanol. Finally, the washed powder was dried and ready for use.

3. Results and discussion

3.1 Synthesis and characterization of nanocomposites

In this study, the UiO-66 series of MOFs were selected as the matrix of the nanocomposites due to their excellent stability and tunable functional groups.[26–28] The target composites were synthesized by a one-step method, which was performed as follows: an appropriate amount of ligand-free UCNPs was directly added to the precursor solution of MOFs, and the mixed solution was subsequently placed in an oven at 120 °C for 24 h. In addition, a series of pure MOFs were prepared as a control.

X-ray diffraction (XRD) patterns (Fig. 1a) illustrated that the synthesized MOFs were all isomorphic to the simulated UiO-66. The diffraction peaks of composites were composed of MOFs and hexagonal UCNPs (JCPDS no. 27-1427). Limited by the distribution of rare earth ions, when MOFs are integrated with core-only UCNPs, the number of rare earth ions capable of interacting with MOFs is relatively small and mainly confined to the surface region of the UCNPs. In order to emphasize the role of MOFs, the UCNPs with a core–shell structure were designed and prepared in this study, in which the core is inert $NaYF_4$ and the shell layer is $NaYF_4$ co-doped with Yb^{3+}/Er^{3+}. The core–shell structure increases the local concentration of active rare earth ions in the shell layer through spatial segregation, which enhances the interaction with MOFs.[29,30]

The morphologies and sizes of the $NaYF_4$ core and Y@98Yb core–shell NPs were characterized by transmission electron microscopy (TEM) (Fig. 1b and c). The TEM images of Y@60Yb and Y@80Yb are shown in Fig. S1.† The diameter of $NaYF_4$ NPs is about 10 nm, while the size of the prepared core–shell Y@98Yb NPs is approximately 16 nm. TEM and high-resolution TEM (HRTEM) images (Fig. 1d and e), together with scanning TEM (STEM) (Fig. 1f) and elemental mapping images of the nanocomposites (Fig. 1g–l), further confirmed the successful synthesis of UiO-66-NH_2@Y@98Yb and the uniform distribution of the UCNPs in the composites. As revealed by Fig. 1e, the observed crystal face distance of the UCNPs on the MOF surfaces was 0.51 nm, which coincides with the (100) crystal face distance of β-$NaYbF_4$. This confirmed both the consistency of the crystal structure of UCNPs with β-$NaYbF_4$ and the successful preparation of the composites.

In order to deeply investigate the role of MOFs in modulating the optical properties of UCNPs, a series of UiO-66 isomers with different functional group side chains were used in this study to complex with UCNPs containing different Yb^{3+} contents. As shown in Fig. 2a–c, the scanning electron microscopy (SEM) images of the synthesized UiO-66, UiO-66-NDC, and UiO-66-NH_2 all exhibited an octahedral structure with smooth surfaces. The SEM images of the composites (Fig. 2d–f and S2†) showed that the UCNPs achieved a homogeneous dispersion on the surfaces of the MOFs. The above results confirmed the generality of the method employed to complex NPs containing different Yb contents with UiO-66 type MOFs.[31] It is worth noting that no significant changes were observed in the crystal structures, morphologies and sizes of UCNPs before and after the composite formation, according to the XRD patterns and TEM and SEM images (Fig. 1a, c, and 2d–f). Moreover, the attachment of the NPs to the surfaces of the MOFs during the growth of the composites retarded the adsorption of

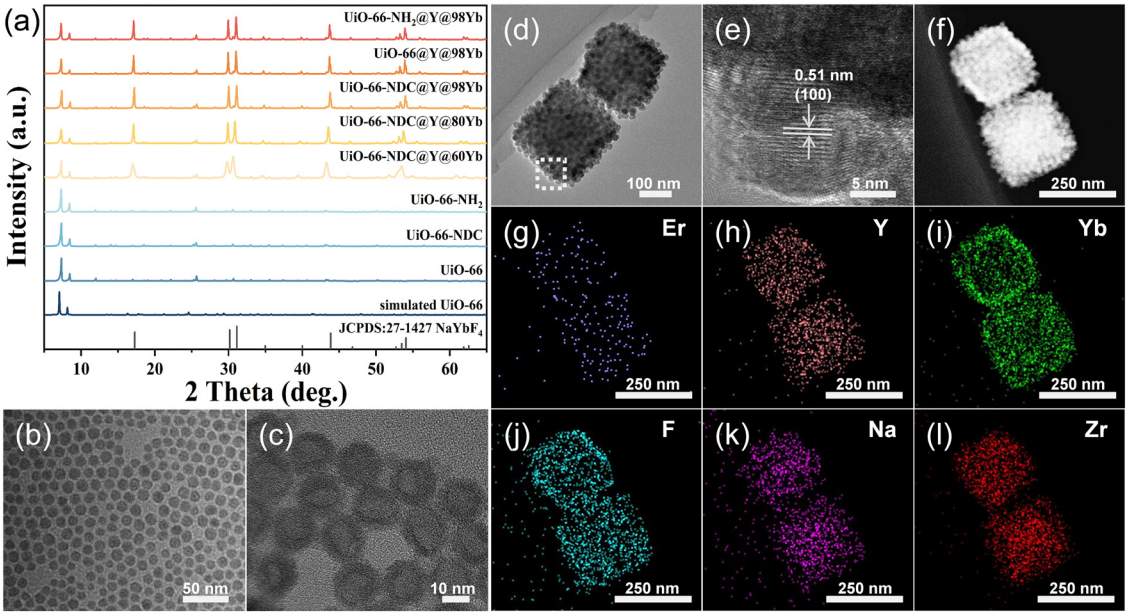

Fig. 1 (a) PXRD patterns of different UiO-66-type MOFs and different composites. The TEM images of (b) core-only $NaYF_4$ NPs, (c) core–shell $NaYF_4$@$NaYbF_4$:2%Er NPs, and (d) the UiO-66-NH_2@$NaYF_4$@$NaYbF_4$:2%Er composite. (e) HRTEM image of the dashed box region in (d). (f) STEM image of the UiO-66-NH_2@$NaYF_4$@$NaYbF_4$:2%Er composite. (g–l) Corresponding element mapping of the UiO-66-NH_2@$NaYF_4$@$NaYbF_4$:2%Er composite shown in (f).

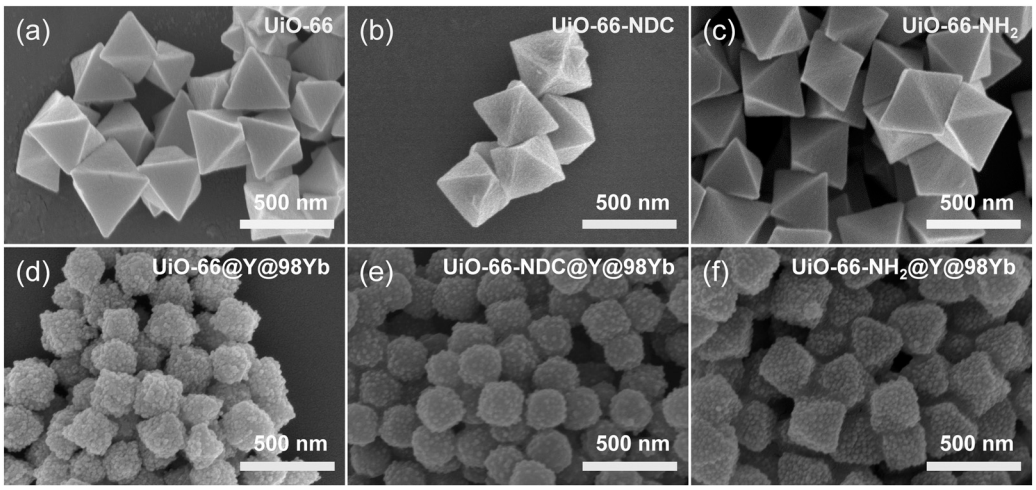

Fig. 2 SEM images of (a–c) pure UiO-66-type MOFs and (d–f) the composites of $NaYF_4$@$NaYbF_4$:2%Er integrated with different MOFs.

precursors, and thus the average particle size of the MOFs decreased after complexing with UCNPs (Fig. 2).[32]

3.2 Influence of excitation power density and MOFs on UCL of nanocomposites

For all optical tests, both the composites and the pure UCNPs were used as dried powder samples. The pure UCNPs were centrifuged and dried to use directly in the tests without any other treatment.

Fig. 3a shows the spectra of UiO-66-NH_2@Y@98Yb as a function of excitation power density. It can be seen that the luminescence intensity at wavelengths of 525 nm, 541 nm and 655 nm all showed an increasing trend with the increase of excitation power density. However, there was a difference in the rate of enhancement between red (655 nm) and green (525 nm and 541 nm) UCL intensity, as shown in Fig. S3,† resulting in a variation of the R/G ratios and the UCL colors with the excitation power density.

In this study, by tuning the excitation power density, we observed a significant difference in LCT performances between the composites and pure UCNPs. When comparing the properties of pure UCNPs with UiO-66-NH_2@Y@98Yb, we found that the R/G ratios of the composite were significantly enhanced, displaying a stronger tendency to emit red luminescence at the same excitation power density (Fig. 3b).

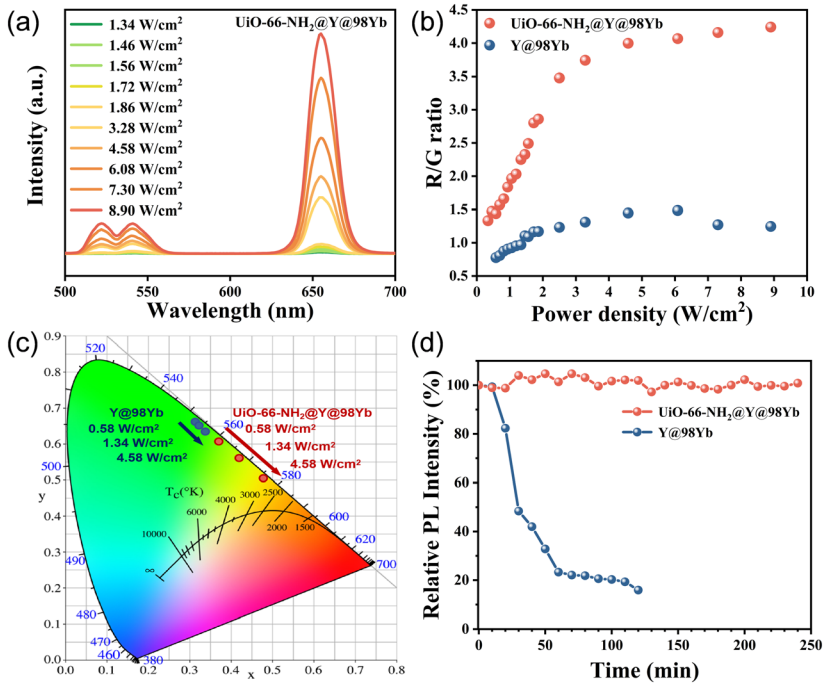

Fig. 3 (a) The UCL spectra of the UiO-66-NH_2@$NaYF_4$@$NaYbF_4$:2%Er composite and (b) R/G ratios of the UiO-66-NH_2@$NaYF_4$@$NaYbF_4$:2%Er composite and $NaYF_4$@$NaYbF_4$:2%Er NPs at different excitation power densities. (c) Corresponding CIE chromaticity coordinates of the UiO-66-NH_2@$NaYF_4$@$NaYbF_4$:2%Er composite and $NaYF_4$@$NaYbF_4$:2%Er NPs at excitation power densities of 0.58 W cm^{-2}, 1.34 W cm^{-2} and 4.58 W cm^{-2}, respectively. (d) Plot of relative PL intensity of the UiO-66-NH_2@$NaYF_4$@$NaYbF_4$:2%Er composite and $NaYF_4$@$NaYbF_4$:2%Er NPs as a function of time under the irradiation of a 980 nm continuous laser with an excitation power density of 4.58 W cm^{-2}.

Specifically, when the excitation power density was increased from 0.34 W cm^{-2} to 2.51 W cm^{-2}, the R/G ratio of UiO-66-NH_2@Y@98Yb increased dramatically from 1.33 to 3.48, whereas that of Y@98Yb only increased from 0.78 to 1.23. By further enhancing the excitation power density to 4.58 W cm^{-2}, the R/G ratio of the composite tended to be saturated, and the saturation value is approximately 4.24. In contrast, the maximum R/G ratio of Y@98Yb under the experimental conditions of this study is only 1.48, a value significantly lower than that of UiO-66-NH_2@Y@98Yb. Fig. 3c clearly demonstrates the difference in LCT performances between UiO-66-NH_2@Y@98Yb and Y@98Yb under the same excitation conditions. The UCL color of the composites was able to gradually shift from yellowish-green to orange-red; in contrast, that of the pure UCNPs remained almost unchanged in the green range.

Typically, pure UCNPs require excitation power densities of several W cm^{-2} to several tens of W cm^{-2} to exhibit significant LCT performance; however, powdered UCNPs are poorly stabilized, which limits the range of applications and often requires colloidization to improve stability. In this work, we also carried out comparative tests on the stability of powdered composites and pure UCNPs by exposing the Y@98Yb and UiO-66-NH_2@Y@98Yb samples to continuous irradiation of a 980 nm continuous laser with an excitation power density of 4.58 W cm^{-2} and monitoring the change of the intensity of the red UCL. Fig. 3d demonstrates the trend of the relative photoluminescence (PL) intensity of the composite and pure UCNPs with irradiation time. The observed results showed that the luminescence intensity of the composite basically remained stable after 240 min of irradiation, displaying excellent photostability. In contrast, that of the UCNPs retained only about 48.4% of its initial intensity after 30 minutes of irradiation and further decreased to about 15.9% after 120 minutes.

Generally speaking, UCNPs are not stable enough and tend to aggregate due to their high surface energy, which leads to a quenching effect of upconversion luminescence.[33,34] Moreover, as the size of UCNPs decreases, their surface-to-volume ratio increases and so do the surface defects, thus exacerbating the surface quenching phenomenon.[35] Fortunately, when NPs were complexed with MOFs, the NPs attached to the surface of MOFs exhibited a self-limiting behavior, leading to effective dispersion of NPs.[31,36] At the same time, this complexation may have passivated the surface defects of UCNPs to some extent.[37] And hence the passivating effect of surface defects and the effective dispersion of the UCNPs may be the factors in enhancing the photostability of the composites.

To further investigate the mechanism of LCT variation in the UiO-66-NH_2@Y@98Yb complex, the advantage of the functional group tolerance of UiO-66-type MOFs was utilized. This was combined with crystal engineering to introduce different vibrational bonds in UiO-66-type MOFs, in order to study their effects on internal energy transfer and multiphonon relaxation (MPR). In analyzing the data shown

in Fig. 4a, we noted that the growth of the R/G ratios for all samples was first faster and then slower with the increase of the excitation power density. Over the range of excitation power densities in this work, the UiO-66-NH_2@Y@98Yb composite had the largest R/G ratio of about 4.24, while that of the UiO-66-NDC@Y@98Yb and UiO-66@Y@98Yb composites was 2.63 and 2.13, respectively, all of which were higher than the maximum R/G ratio of Y@98Yb of 1.49. Moreover, it was noticed in this work that the R/G ratios of pure UCNPs exhibited a slightly decreasing trend at the later stage of the variation with increasing excitation power density. This phenomenon may originate from the significant decay of their stability under high excitation power density as mentioned previously. Fig. 4b illustrates the comparison of the red UCL intensity of Y@98Yb and its composites with three different UiO-66-type MOFs under 980 nm continuous laser irradiation (excitation power density of 4.58 W cm^{-2}) after normalization of the green UCL intensity at 541 nm. To be specific, UiO-66-NH_2@Y@98Yb showed the most significant performance in terms of red UCL enhancement. Its red UCL emission intensity was about 2.44 times that of Y@98Yb. And the enhancement factor of UiO-66-NDC@Y@98Yb and UiO-66@Y@98Yb was 1.41 and 1.09, respectively. By comparing the data in Fig. 4a and b, it is clearly observed that UiO-66-type MOFs had a general enhancement effect on the R/G ratios of UCNPs. Furthermore, under otherwise identical conditions, MOFs with different side groups exhibited significant differences in their effects on the R/G ratios of UCNPs. In addition, an important phenomenon was noted in this study: the maximum R/G ratios of Y@60Yb, Y@80Yb, and Y@98Yb as well as those of the three composites integrated with the UCNPs with different Yb contents and UiO-66-NDC showed an increasing trend with the increase of Yb contents in the shell layer (Fig. S4† and 4a).

In order to exclude that the increase in the R/G ratios of the composites is due to the absorption of green UCL from the UCNPs by MOFs, we also tested the UV-vis absorption spectra of different MOFs. From Fig. S5,† we observe that MOFs do not exhibit significant absorption characteristics within the emission band of UCNPs prepared in this work. This finding effectively excluded that the above mentioned reason may have led to the increase in the R/G ratios of the composites. Based on these findings, Fig. 4c demonstrates the related UC mechanism. The reason for the variation of the R/G ratios and the UCL colors with the excitation power density is that in UCNPs with a higher Yb^{3+} content, the cross-relaxation (CR) process between Yb^{3+} and Er^{3+}: Er^{3+} ($^4G_{11/2}$) + Yb^{3+} ($^2F_{7/2}$) → Er^{3+} ($^4F_{9/2}$) + Yb^{3+} ($^2F_{5/2}$) takes place much more easily. Meanwhile, when the excitation power density is further increased, route II tends to dominate in the emission process of Er^{3+} rather than route I for the transition

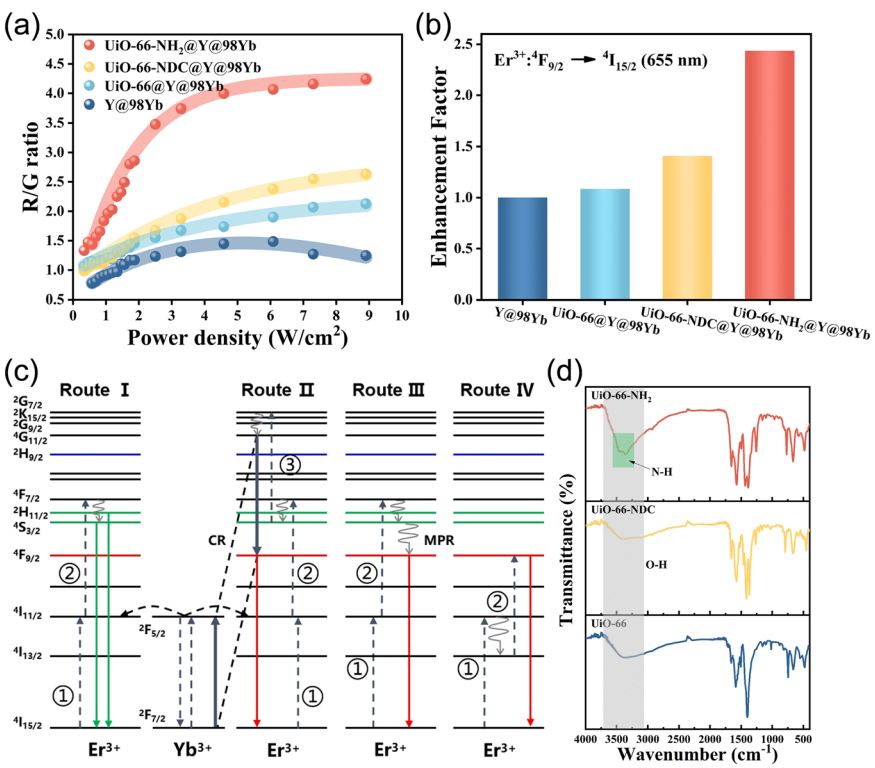

Fig. 4 (a) Variation of R/G ratios of $NaYF_4$@$NaYbF_4$:2%Er and its composites with different UiO-66-type MOFs at different excitation power densities. (b) Luminescence enhancement factors of UiO-66-type-MOFs@$NaYF_4$@$NaYbF_4$:2%Er relative to pure $NaYF_4$@$NaYbF_4$:2%Er NPs at Er^{3+}: $^4F_{9/2}$ → $^4I_{15/2}$ (655 nm) after normalization to UCL at 541 nm at an excitation power density of 4.58 W cm^{-2}. (c) The proposed mechanisms of UC red and green emission in Yb^{3+}/Er^{3+} co-doped $NaYF_4$ NPs. (d) FTIR spectra of different UiO-66-type MOFs.

paths of the electrons at the $^2H_{11/2}/^4S_{3/2}$ levels. The energy gap from both the green-emitting levels ($^2H_{11/2}/^4S_{3/2}$) to the red-emitting level ($^4F_{9/2}$) measures approximately 3200 cm^{-1}, and that between the $^4I_{11/2}$ and $^4I_{13/2}$ energy levels is approximately 3600 cm^{-1}, both of which can be bridged by coupling the vibrations in organic stretching vibration. And hence chemical bonds with high-energy vibrations help to promote the $^2H_{11/2}/^4S_{3/2} \rightarrow {}^4F_{9/2}$ and $^4I_{11/2} \rightarrow {}^4I_{13/2}$ MPR processes of Er^{3+} in route III and route IV, thereby suppressing the electronic transitions at the $^2H_{11/2}/^4S_{3/2}$ level through non-radiative deactivation.[7,38–40] However, they do not appear to have a significant effect on the population of the $^4F_{9/2}$ level of Er^{3+}.[41] In this study, we tested the UCL lifetimes of the pure UCNPs and composites at 541 nm and 655 nm (Fig. S6†). The experimental results showed that when UCNPs complexed with MOFs, the chemical bonds with high-energy vibration that may exist inside the MOFs attenuated both the green and red UCL lifetimes of the UCNPs. In particular, this attenuation effect was more significant on the green UCL lifetimes.

Based on the above experimental results, the three UiO-66-type MOFs and their corresponding ligands were further analyzed by Fourier transform infrared spectroscopy (FTIR) in this study (Fig. 4d and S7†). The results showed that all three MOFs exhibited strong absorption peaks located in the range of 3200–3700 cm^{-1}, corresponding to O–H bonds with high-energy vibrations. As a result, after the complexation with UiO-66-type MOFs, the UCNPs tended to emit red luminescence and the R/G ratios were significantly enhanced due to the O–H bonds with high-energy vibrations in the structure of MOFs. It is noteworthy that UiO-66-NH_2 has additional N–H bonds in addition to the O–H bonds, which further facilitates the MPR processes. Therefore, under otherwise identical conditions, UiO-66-NH_2@Y@98Yb had the highest red enhancement factor and R/G ratio compared to the other composites in this study.

The efficient LCT emission in UiO-66-NH_2@Y@98Yb is advantageous for multilevel anti-counterfeiting due to the significant change in luminescence color with only a small variation in excitation intensity. This property enables the creation of intricate and difficult-to-replicate security features, enhancing the overall robustness of anti-counterfeiting measures. As a proof-of-concept experiment, we prepared security labels by coating two materials, Y@98Yb and UiO-66-NH_2@Y@98Yb, onto non-fluorescent labels, with Y@98Yb as the upper dot and UiO-66-NH_2@Y@98Yb as the lower dot (Fig. 5). Then we gradually increased the excitation power density and recorded the luminescence color changes of the two dots under the same experimental conditions. The results showed that with the increase of the excitation power density, the luminescence color of the upper dot basically remained green, while the lower dot gradually changed from yellowish-green to orange-red. This result proved the significant advantages of MOFs@UCNPs in multilevel anti-counterfeiting.

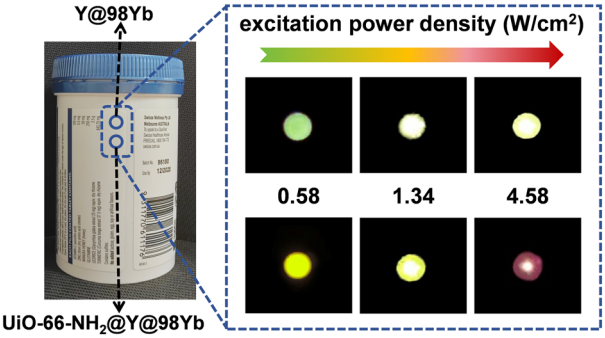

Fig. 5 Multilevel anti-counterfeiting application of Y@98Yb and UiO-66-NH_2@Y@98Yb.

4. Conclusion

In summary, Yb^{3+}/Er^{3+} co-doped core–shell UCNPs were successfully integrated with UiO-66-type MOFs in this study by an *in situ* synthesis strategy. The UCNPs achieved uniform dispersion on the surfaces of MOFs. And their UCL performance was effectively tuned by MOFs, where the R/G ratios were significantly enhanced and the UCL tended towards red emission at the same excitation power density. Under the established experimental conditions, the maximum R/G ratio of Y@98Yb was 1.49, while that of UiO-66-NH_2@Y@98Yb was increased to 4.24. This phenomenon is attributed to the chemical bonds with high-energy vibrations in the MOFs that promote the MPR processes of $^2H_{11/2}/^4S_{3/2} \rightarrow {}^4F_{9/2}$ and $^4I_{11/2} \rightarrow {}^4I_{13/2}$ of Er^{3+}, which enhance the red UCL emission at the expense of the green ones. The UCL colors of UiO-66-NH_2@Y@98Yb could change from yellowish-green to orange-red with the increase of power density. In addition, the photostability of the composites was superior to that of UCNPs. This work provides a novel exogenous strategy for regulating the UCL properties of UCNPs, which is expected to provide a more suitable solution for specific applications.

Data availability

All data included in this study are available upon request by contact with the corresponding author.

Author contributions

Huiwen Yan: conceptualization, methodology, data curation, and writing. Wenqian Cao: conceptualization, methodology, and writing – review & editing. Zhiyu Wang: morphology characterization. Yuanjing Cui and Guodong Qian: supervision, funding acquisition, project administration, and writing – review & editing.

Conflicts of interest

There are no conflicts to declare.

Acknowledgements

This work was supported by the National Natural Science Foundation of China (52025131), the National Key R&D Program of China (2022YFB3503703), and the Science Technology Department of Zhejiang Province (2024C01191).

Notes and references

1 Y. Liu, Y. Lu, X. Yang, X. Zheng, S. Wen, F. Wang, X. Vidal, J. Zhao, D. Liu, Z. Zhou, C. Ma, J. Zhou, J. A. Piper, P. Xi and D. Jin, *Nature*, 2017, **543**, 229–233.
2 W. Ren, G. Lin, C. Clarke, J. Zhou and D. Jin, *Adv. Mater.*, 2020, **32**, 1901430.
3 J. Zhou, A. I. Chizhik, S. Chu and D. Jin, *Nature*, 2020, **579**, 41–50.
4 S. Mei, J. Zhou, H.-T. Sun, Y. Cai, L.-D. Sun, D. Jin and C.-H. Yan, *Adv. Sci.*, 2021, **8**, 2003325.
5 J. Zhou, Q. Liu, W. Feng, Y. Sun and F. Li, *Chem. Rev.*, 2015, **115**, 395–465.
6 G. Bai, M.-K. Tsang and J. Hao, *Adv. Funct. Mater.*, 2016, **26**, 6330–6350.
7 M. Kraft, C. Würth, V. Muhr, T. Hirsch and U. Resch-Genger, *Nano Res.*, 2018, **11**, 6360–6374.
8 M. T. Berry and P. S. May, *J. Phys. Chem. A*, 2015, **119**, 9805–9811.
9 M. Kaiser, C. Würth, M. Kraft, T. Soukka and U. Resch-Genger, *Nano Res.*, 2019, **12**, 1871–1879.
10 B. Shen, S. Cheng, Y. Gu, D. Ni, Y. Gao, Q. Su, W. Feng and F. Li, *Nanoscale*, 2017, **9**, 1964–1971.
11 F. Wang and X. Liu, *J. Am. Chem. Soc.*, 2008, **130**, 5642–5643.
12 J. Wang, R. Deng, M. A. MacDonald, B. Chen, J. Yuan, F. Wang, D. Chi, T. S. A. Hor, P. Zhang, G. Liu, Y. Han and X. Liu, *Nat. Mater.*, 2014, **13**, 157–162.
13 W. You, D. Tu, R. Li, W. Zheng and X. Chen, *Nano Res.*, 2019, **12**, 1417–1422.
14 M. Dong, X. Li, F. Chi, X. Wei, M. Yin and Y. Chen, *J. Rare Earths*, 2017, **35**, 629–636.
15 J. Lü, J. Liang, T. Fan, Y. Zhou, T. Deng and W. Li, *J. Lumin.*, 2024, **271**, 120594.
16 A. Hlaváček, Z. Farka, M. J. Mickert, U. Kostiv, J. C. Brandmeier, D. Horák, P. Skládal, F. Foret and H. H. Gorris, *Nat. Protoc.*, 2022, **17**, 1028–1072.
17 C. Jia, T. He and G.-M. Wang, *Coord. Chem. Rev.*, 2023, **476**, 214930.
18 D.-G. Ha, R. Wan, C. A. Kim, T.-A. Lin, L. Yang, T. Van Voorhis, M. A. Baldo and M. Dincă, *Nat. Mater.*, 2022, **21**, 1275–1281.
19 X. Zhao, Y. Wang, D.-S. Li, X. Bu and P. Feng, *Adv. Mater.*, 2018, **30**, 1705189.
20 Y. Cui, B. Li, H. He, W. Zhou, B. Chen and G. Qian, *Acc. Chem. Res.*, 2016, **49**, 483–493.
21 S. T. Meek, J. A. Greathouse and M. D. Allendorf, *Adv. Mater.*, 2011, **23**, 249–267.
22 H. R. Moon, D.-W. Lim and M. P. Suh, *Chem. Soc. Rev.*, 2013, **42**, 1807–1824.
23 M. Zhao, K. Yuan, Y. Wang, G. Li, J. Guo, L. Gu, W. Hu, H. Zhao and Z. Tang, *Nature*, 2016, **539**, 76–80.
24 Q.-L. Zhu, J. Li and Q. Xu, *J. Am. Chem. Soc.*, 2013, **135**, 10210–10213.
25 I. Ahmed, M. M. H. Mondol, M. J. Jung, G. H. Lee and S. H. Jhung, *Coord. Chem. Rev.*, 2023, **475**, 214912.
26 F. Ahmadijokani, H. Molavi, M. Rezakazemi, S. Tajahmadi, A. Bahi, F. Ko, T. M. Aminabhavi, J.-R. Li and M. Arjmand, *Prog. Mater. Sci.*, 2022, **125**, 100904.
27 D. Li, S.-H. Yu and H.-L. Jiang, *Adv. Mater.*, 2018, **30**, 1707377.
28 W. Zhang, G. Lu, C. Cui, Y. Liu, S. Li, W. Yan, C. Xing, Y. R. Chi, Y. Yang and F. Huo, *Adv. Mater.*, 2014, **26**, 4056–4060.
29 K. R. Mun, J. Kyhm, J. Y. Lee, S. Shin, Y. Zhu, G. Kang, D. Kim, R. Deng and H. S. Jang, *Nano Lett.*, 2023, **23**, 3014–3022.
30 D. Xu, J. Xu, X. Shang, S. Yu, W. Zheng, D. Tu, R. Li and X. Chen, *CCS Chem.*, 2021, **4**, 2031–2042.
31 Z. Yuan, L. Zhang, S. Li, W. Zhang, M. Lu, Y. Pan, X. Xie, L. Huang and W. Huang, *J. Am. Chem. Soc.*, 2018, **140**, 15507–15515.
32 W. Xu, L. Lei, Y. Wang, P. N. Prasad, L. Chen and S. Xu, *Laser Photonics Rev.*, 2023, **17**, 2200997.
33 M. A. Boles, D. Ling, T. Hyeon and D. V. Talapin, *Nat. Mater.*, 2016, **15**, 141–153.
34 A. Schroter, S. Märkl, N. Weitzel and T. Hirsch, *Adv. Funct. Mater.*, 2022, **32**, 2113065.
35 H. Xu, S. Han, R. Deng, Q. Su, Y. Wei, Y. Tang, X. Qin and X. Liu, *Nat. Photonics*, 2021, **15**, 732–737.
36 M. Gutiérrez, Y. Zhang and J.-C. Tan, *Chem. Rev.*, 2022, **122**, 10438–10483.
37 H. Wu, L. Yao, W. Cao, Y. Yang, Y. Cui, D. Yang and G. Qian, *J. Mater. Chem. C*, 2022, **10**, 5550–5558.
38 R. Arppe, I. Hyppänen, N. Perälä, R. Peltomaa, M. Kaiser, C. Würth, S. Christ, U. Resch-Genger, M. Schäferling and T. Soukka, *Nanoscale*, 2015, **7**, 11746–11757.
39 I. Hyppänen, N. Höysniemi, R. Arppe, M. Schäferling and T. Soukka, *J. Phys. Chem. C*, 2017, **121**, 6924–6929.
40 L. F. Scatena, M. G. Brown and G. L. Richmond, *Science*, 2001, **292**, 908–912.
41 X. Xue, S. Uechi, R. N. Tiwari, Z. Duan, M. Liao, M. Yoshimura, T. Suzuki and Y. Ohishi, *Opt. Mater. Express*, 2013, **3**, 989–999.